Design and Development of a Seamless Smart Morphing Wing Using Distributed Trailing Edge Camber Morphing for Active Control

Mkhoyan, T.; Thakrar, N.R.; De Breuker, R.; Sodja, J.

DOI
10.2514/6.2021-0477

Publication date
2021

Document Version
Final published version

Published in
AIAA Scitech 2021 Forum

AIAA SciTech Forum
11–15 & 19–21 January 2021, VIRTUAL EVENT
AIAA Scitech 2021 Forum

10.2514/6.2021-0477

Design and Development of a Seamless Smart Morphing Wing Using Distributed Trailing Edge Camber Morphing for Active Control

Tigran Mkhoyan*, Nisarg R. Thakrar †, Roeland De Breuker‡, Jurij Sodja§
Delft University of Technology, Delft, The Netherlands

In this study, the design and development of an autonomous morphing wing concept were investigated. The morphing wing was developed in the scope of the Smart-X project, aiming to demonstrate in-flight performance optimisation. This study proposed a novel distributed morphing concept, with six Translation Induced Camber (TRIC) morphing trailing edge modules, interconnected with triangular skin segments joined by an elastomer material to allow seamless variation of local lift distribution along the wingspan. A FSI structural analysis tool was developed, to achieve a feasible design, capable of reaching target shapes and minimising the actuation loads with fibreglass weave material. A conventional actuator and kinematic mechanism were selected such that both static and dynamic requirements in terms of bandwidth, actuation force and stroke were fulfilled. The integration of smart sensing technologies and active morphing design developed for the Smart-X wing is facilitated in static and dynamic wind-tunnel tests at the Open Jet Facility (OJF) at the Delft University of technology, with multi-objective control of the active morphing system.

I. Introduction

The advancements in aircraft materials, manufacturing technology, controller and hardware design allow developing increasingly flexible aircraft concepts. Generally, the flexibility comes as a side effect of lighter aircraft design and needs to be adequately accounted for, however, a more natural approach is to utilise the flexibility for the benefit of better performance, much like it is seen in nature with wing morphing for better gliding performance [1, 2]. As in nature, morphing wing concepts have been evolving since the early years of the aviation. One of the well-documented examples was the active roll control of the Wright Flyer, the first successful heavier-than-air powered aircraft. In this lightweight design, the lateral stability was ensured by wing twist-warping [3]. This was possible because the flexible fabric-wrapped structure was well suited for morphing. As the flight speeds and loads were increased with the advancement of flight, a stiffer wing was required to fulfil structural requirements and to overcome aeroelastic instabilities. As a result, the considerably stiffer wing design - generally optimised for cruise conditions - is faced with the compromised performance at other flight conditions. Active morphing has the potential to reduce this performance loss and to improve aircraft performance across the flight envelope. In literature, various morphing concepts can be found each with their advantages and disadvantages [4].

A comprehensive review of early morphing concepts is found in [5], presenting various combinations of actuator material selections, actuator mechanisms and skin types. The concepts vary from conventional to compliant mechanisms and materials. Various actuator options are investigated, ranging from conventional to piezoelectric or shape memory alloys. The morphing can be applied to the leading edge, trailing edge or both. Several other concepts [6–8] achieve low actuation force by utilising compliant skin and actuation mechanism. While promising, the studies highlight the importance of further research into manufacturing and up-scaling of complex compliant designs, as currently, the manufacturing process of them is challenging. Further examples of compliant mechanisms are investigated in the literature combined with conventional actuators (Previtali et al) [7, 9] and piezoelectric skin actuation (Molinari et

*Ph.D. student, Faculty of Aerospace Engineering, Aerospace Structures and Materials department, T.Mkhoyan@tudelft.nl, P.O. Box 5058, 2600GB Delft, The Netherlands.
†M.S.c, Faculty of Aerospace Engineering, Aerospace Structures and Materials department, N.R.Thakrar@student.tudelft.nl, P.O. Box 5058, 2600GB Delft, The Netherlands
‡Associate Professor, Faculty of Aerospace Engineering, Aerospace Structures & Computational Mechanics, R.DeBreuker@tudelft.nl, P.O. Box 5058, 2600GB Delft, The Netherlands
§Senior researcher, Faculty of Aerospace Engineering, Aerospace Structures & Computational Mechanics, J.Sodja@tudelft.nl, P.O. Box 5058, 2600GB Delft, The Netherlands

al.) [8, 10]. Recent studies also investigated the use of ultralight, lattice-based, structures assembled in a modular adaptive structure. The advantage is that these materials can have the stiffness of a typical elastomer at the mass-density typical to aero-gel [11], [12]. In the latter study, improved aerodynamic efficiency and roll control authority with spatially programmed elastic morphing shape is demonstrated. However, additional consideration is needed to ensure flexibility of the structure while reserving the room for fuel, batteries and/or additional components to be installed in the wing. The literature survey suggests that many morphing concepts are restricted to either twist or camber morphing mechanisms, and propose a complex mechanism that introduces manufacturing challenges or consumes a large portion of the internal volume. Furthermore, many concepts propose a global morphing approach, while in the scope of active control, a distributed and over-actuated control surface layout is necessary to apply simultaneous load alleviation, flutter suppression and drag minimisation. In a recent study for the EU FP7 CHANGE project, a morphing concept called the Translation Induced Camber (TRIC), is introduced to address some of these problems [13]. This concept implements a relatively simple and effective morphing mechanism that uses a combination of cross-sectional warping and skin bending to induce both camber and twist morphing. The concept has the advantage that conventional actuators can be used due to its relatively simple and compact design, and significant space can be reserved inside the main wingbox, for fuel and installation of additional auxiliary systems. The main disadvantage of this concept is that the morphing is global across the span, since the control is governed by only two pairs of actuators for the trailing edge and the leading edge, respectively. This prevents local control of camber or twist distribution across the span.

To address this problem, the current study extends on the TRIC concept. It introduces a distributed modular morphing design, where adjacent morphing modules are connected with elastomeric skin to allow seamless variation of local lift distribution along the wingspan. This morphing design, developed as an autonomous smart wing concept, called the SmartX wing, aims to demonstrate an integrated and coherent approach towards multi-objective load alleviation, flutter suppression and performance optimisation of adaptive aircraft wings.

II. SmartX: The smart morphing wing

The aim of the SmartX is to demonstrate in-flight performance optimisation of several objectives such as (i) drag optimisation, (ii) load alleviation, (iii) flutter suppression and (iv) shape control through multidisciplinary integration of control, sensing and morphing design. The high-level control and sensor strategy of the SmartX concept are presented in Fig. 1. Several key components of the diagram are:

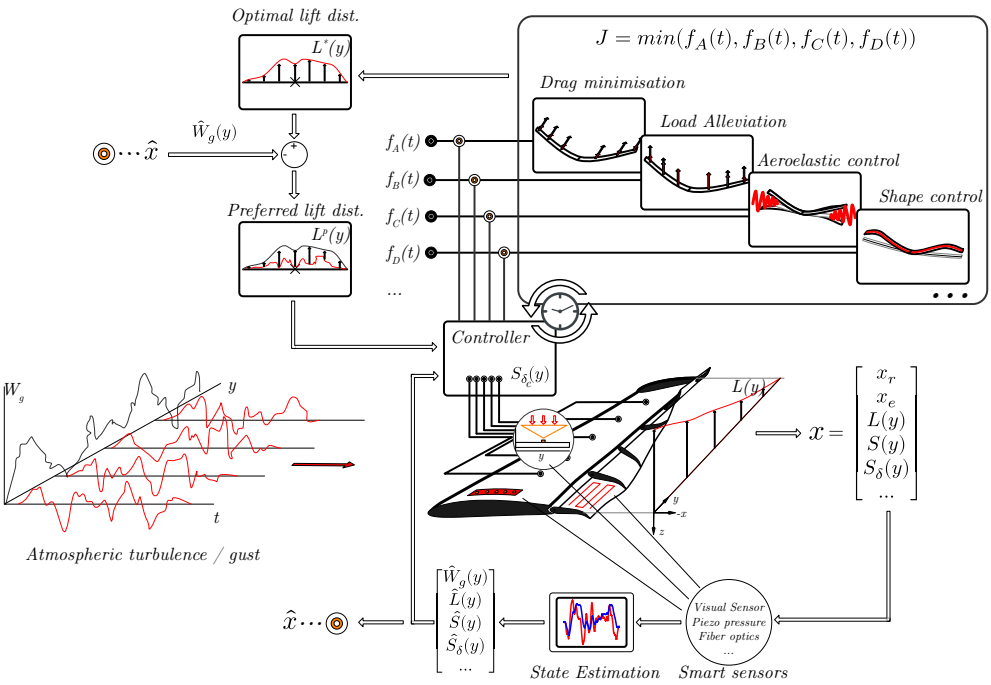

Fig. 1 The SmartX concept.

- In the center, the wing is displayed with the continuously morphing trailing edge.
- Integrated actuators morph the trailing edge surface by $S_\delta(y)$.
- Sensors in the wing allow real-time measurements of (i) global shape of the wing with fibre optic sensors, (ii) flow separation and control effectiveness of the morphing surface, using piezoelectric sensors (iii) position feedback of the morphing surfaces using high-speed cameras installed at the root to feed to the controller [14, 15],.
- A multi-objective optimal controller adaptively drives the actuator array towards the desired shape $S_\delta(y)$ curve to optimise in real-time for several objectives such drag minimisation and load alleviation, formulated in the objective function, J
- As the wing encounters gust and varying atmospheric conditions, the controller continuously adapts the morphing surfaces to obtain the optimal lift distribution for the given objectives.

A. The morphing concept

The proposed morphing concept is based on the TRIC morphing concept introduced in [13]. However, in the scope of smart active control, this concept has the disadvantage that the morphing module, with a single pair of actuators, is global across the span. This implies that local camber or twist distribution cannot be commanded along the span, whereas, in the scope of smart integrated multi-objective control, control of local lift distribution is essential. The current study, therefore, extends the TRIC concept to allow for local camber and twist morphing by substituting a single TRIC morphing module along the entire span with several morphing modules which remain connected to each other to maintain a continuous and seamless outer wing skin. In the current case, six such morphing modules are placed along the span. As with the TRIC concept, the skin is actuated internally, allowing smooth and seamless morphing along the chord. As is illustrated in Fig. 2a.

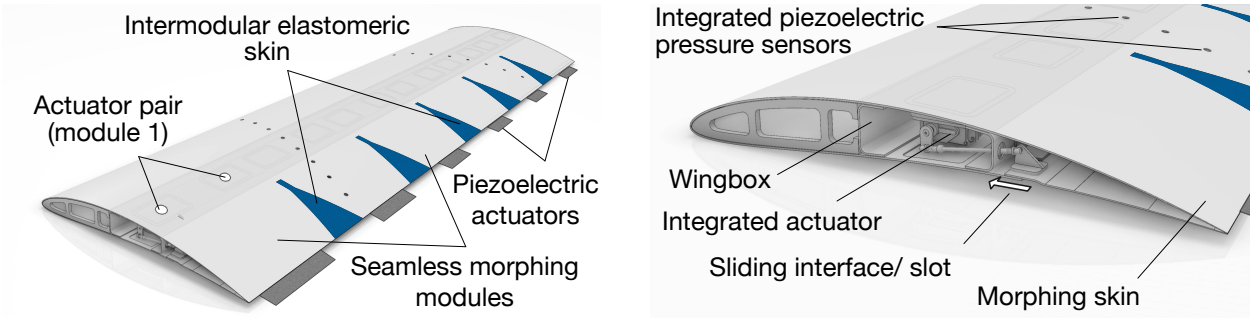

(a) Detailed view of SmartX wing. **(b) Close UP of the TRIC morphing module**

Fig. 2 Overview of the SmartX seamless TRIC morphing concept.

Each module is equipped with two pairs of actuators allowing local symmetric (camber) and asymmetric (twist) morphing. Individual morphing modules are interconnected by an elastomeric skin to allow continuous spanwise variation of the lift distribution between the morphing modules as illustrated in Fig. 2.

The main advantage of the current design is that lift distribution along the span can be locally controlled by individually adjusting the camber and twist of each morphing module, thereby allowing the wing to settle into the most optimal lift to drag ratio (*shape control*) to *minimize drag*. Furthermore, the lift distribution can be adapted to perform *load alleviation* when necessary. Lastly, the trailing edge is equipped with fast piezoelectric bimorph actuators at the morphing trailing edge for *aeroelastic control* (e.g. flutter suppression), hereby covering the targets presented earlier in Fig. 1. To sustain the required loads, meet the actuator constraints and achieve the desired morphing shapes, the composite wing skin is tailored and optimised. Therefore, a Fluid-Structure Interaction (FSI) structural optimisation tool is developed, that allows for (i) fast analysis and (ii) fast optimisation of ply orientation and thickness in terms of the given input loads, desired target shapes and actuator limits.

B. Smart technology integration

The smart sensors actuators and mechanisms, as described in Sec. II, were integrated into the morphing wing. These are composed of state-of-the-art : (i) piezoelectric pressure sensors, (ii) embedded fibre-optic sensors, (iii) seamless morphing control and (iv) and visual tracking system for control feedback [14, 15].

III. Design Methodology

The design of the morphing wing was obtained using an FSI framework, which couples a Finite Element Model (FEM) and an inviscid low-cost aerodynamic model of the morphing system [16].

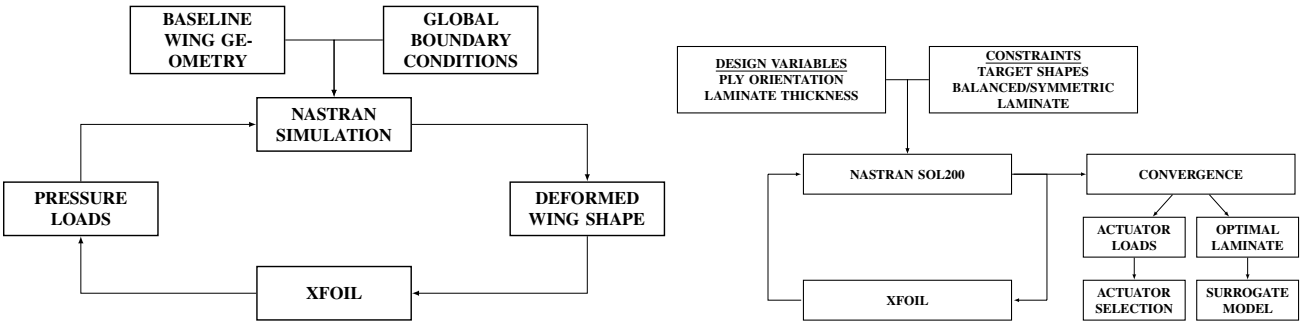

(a) Flow chart of the FSI framework. **(b) Flow chart of the FSI optimisation framework.**

Fig. 3 Design methodology flow diagrams [16]

An overview of the FSI framework and the FSI optimisation process are given in Figures 3a and 3b, respectively. The methodology was developed with two goals in mind: (i) to produce the optimised morphing design presented, capable of meeting the objectives outlined in Sec. II and obtain a surrogate model of the distributed morphing system for active multi-objective control of the physical system in real-time.

The design approach can be summarized in the following steps/elements [16]:

1) Development of an FSI tool and an optimisation routine incorporating the FSI loop, allowing laminate design optimisation by varying the ply thickness to ensure target shapes at minimal input force.
2) Development of easy to manufacture laminate meeting the actuator loads and actuator travel range
3) Selection of the actuator and actuator mechanism.
4) Modular analysis of the entire wing broken down in individual 300mm modules, where the section forward of the rear spar was considered rigid. A rigid wing box and the leading edge was designed to ensure each module operated similarly.

A. FSI analysis and optimisation framework

The analysis and optimisation tool couples a FEM model in NASTRAN [17] and an inviscid aerodynamic model in XFOIL [18] in an analysis loop, which is facilitated via MATLAB. The loop was run iteratively until an equilibrium was reached between the aerodynamic loads and then structural deformations and the analysis converged. Suitable convergence bounds were determined for the deformation error, actuation load and the lift coefficient increment, by performing a convergence study. Convergence of these variables typically reached in three-four iterations [16]. The

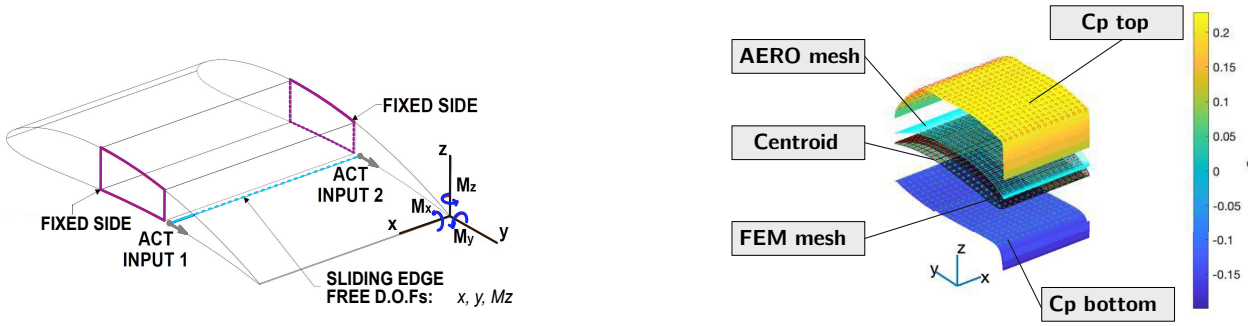

(a) Fem model boundary conditions. **(b) Coupling of the FEM and aerodynamic meshes.**

Fig. 4 FSI components and modeling approach.

inviscid aerodynamic model allowed analysis of angle of attack between -12 and 5 degrees for the given NACA 6510

baseline airfoil shape. The FEM model consisted of a morphing module with a 500 mm cord and 300 mm span. A cut was introduced at the bottom skin to allow translation of the morphing trailing edge according to the TRIC principle. The cut was bridged by an actuator pair installed at each end of the module, with the purpose to (i) provide actuation input (symmetric and asymmetric) and (ii) prevent the skin from moving under exerted aerodynamic loads (re-closing the cross-section). The aerodynamic and structural meshes were coupled by a 2D grid interpolation routine and propagated as pressure loads in the FEM model. Fig. 4 shows the basic principle of the model and mesh coupling.

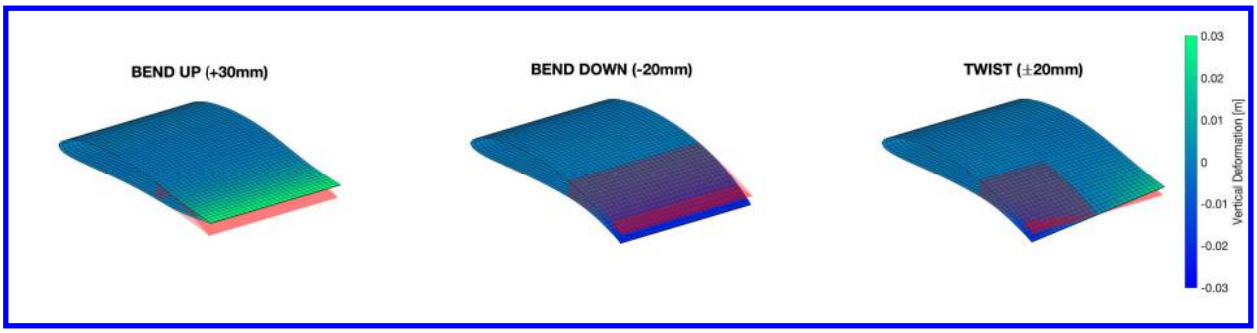

Fig. 5 Deformed morphing surfaces for all sub cases resulting from opimisation routine.

The optimisation routine (shown in Fig. 3b), was designed with the NASTRAN's SOL200 optimiser [19]. The morphing conditions were optimised *simultaneously* as sub-cases in each optimisation run. Three morphing sub-cases cases were considered in the FSI model to analyse morphing behaviour: (i) Bend Up, (ii) Bend Down and (iii) Twist. The primary goal of the optimisation routine was to find an optimal laminate design for the morphing surface with the objective of minimising actuation force for these three morphing conditions.

The tip deflections were constrained for the optimisation at 30,−20 and ±20 mm, respectively. The analysis was carried out at 30 m/s and an angle of attack range of -12 to 5 degrees. The range of deformations was chosen such that a ΔC_L of approximately 0.6 was achieved from baseline C_L at undeformed NACA 6510 condition.

B. Design optimisation outcome

Table 1 Actuator peak forces for various subcases.

Subcase	Act. Force 1 $[N]$	Act. Force 2 $[N]$	Act. 1 Displacement $[mm]$	Act. 2 Displacement. $[mm]$	C_L [-]
Bend Up	61	61	6.5	6.5	-1.7
Bend Down	-60	-60	-4.5	-4.5	2.2
Twist	-50	23	4.5	-4.5	0.85

The deformed morphing surfaces resulting from the optimisation for the three sub-cases are presented in Fig 5. They are superimposed on an undeformed surface to visualise the degree of deformations taking place. The colours represent the relative vertical deformations of the system. The actuator loads and lift increments achieved by morphing changes are listed in Tab. 1.

Fibre-glass designation US 7630 (MIL-Y-1140H) was selected for use in the final design [20]. To produce the laminate design, a ply dropping sequence was implemented and number of plies dropped in the optimisation until the actuator loads and morphing shapes converged. The final ply dropping sequence is shown in Fig. 6a. The heatmap shows the undeformed morphing surface overlayed with the optimised thickness distribution. The colour map shows the number of plies required in each design region to build the morphing surface laminate.

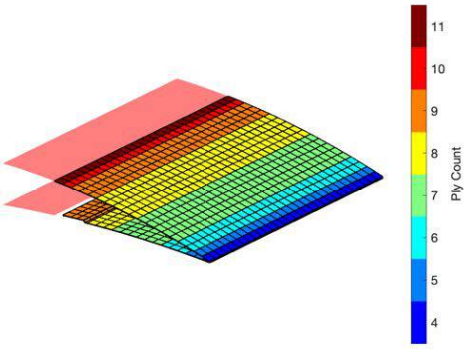

(a) Optimised laminate design and ply dropping sequence.

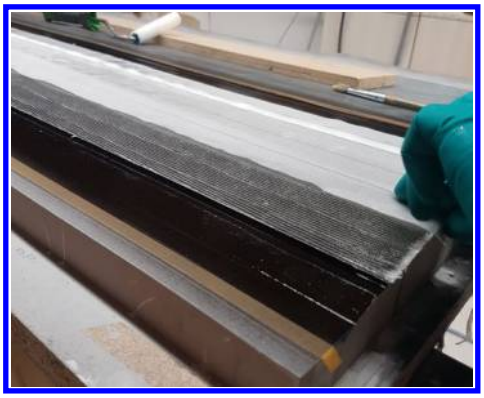

(b) Process of ply dropping fibre glass layers.

Fig. 6 Ply dropping design outcome and manufacturing.

IV. Wing model manufacturing

The wing design developed in section III must be converted to a detailed design suitable for the manufacturing of the wind tunnel demonstrator.

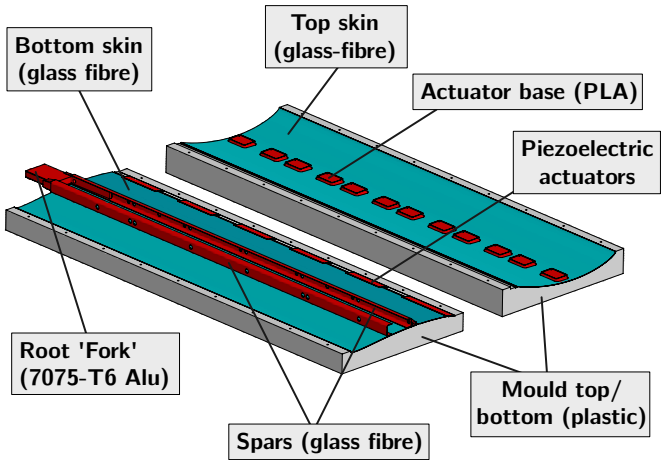

(a) Skin and component manufacturing.

(b) Integrating smart sensors, actuators and components in the wing.

Fig. 7 Integration of smart technologies and assembly.

A. Morphing wing manufacturing and assembly

The resulting morphing wing design was constructed in four parts (i) top skin, (ii) bottom skin and (iii) wing box and spars, (iv) morphing trailing edge (v) spars. The wing skin was constructed with the vacuum curing of wet-laid glass fibre inside two mould parts (top and bottom) as shown in Fig. 7a. The top skin was made in one pass, with the ply dropping incorporated at the trailing edge. The bottom skin was made in two curing steps, the wing box skin and the morphing trailing edge, as a sliding edge needed to be incorporated for the TRIC concept. The spars were cured in a separate mould and assembled in the main wing structure. Once all the components were cured, the sensors and piezo actuators were integrated into the appropriate wing halve and the two halves were joined together. Figures 7 and 8b show the joining process and the assembly of the components, respectively.

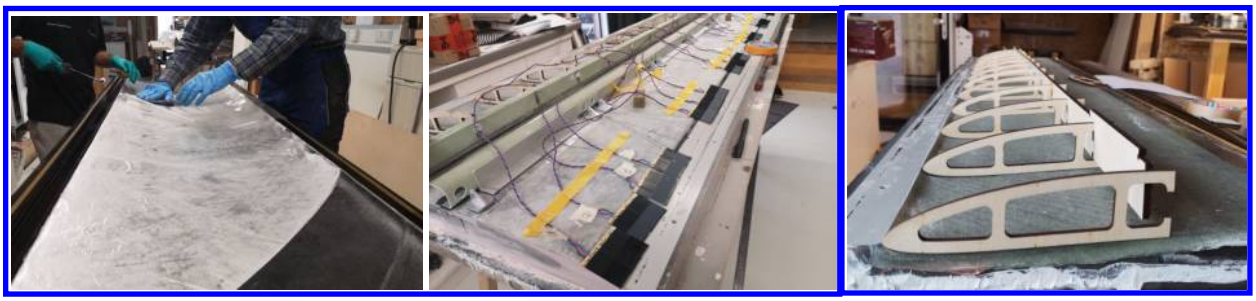

(a) Laminating top skin. (b) Spars and wing components alignment. (c) Rib assembly.

Fig. 8 Manufacturing process and assembly preparation.

B. Actuator selection

To determine the actuator torque requirements and select a suitable actuator, the actuation loads were evaluated for the entire morphing range in the FSI system by incrementing horizontal travel at the actuation points, from -7mm to 7mm (in 1mm increments) and .

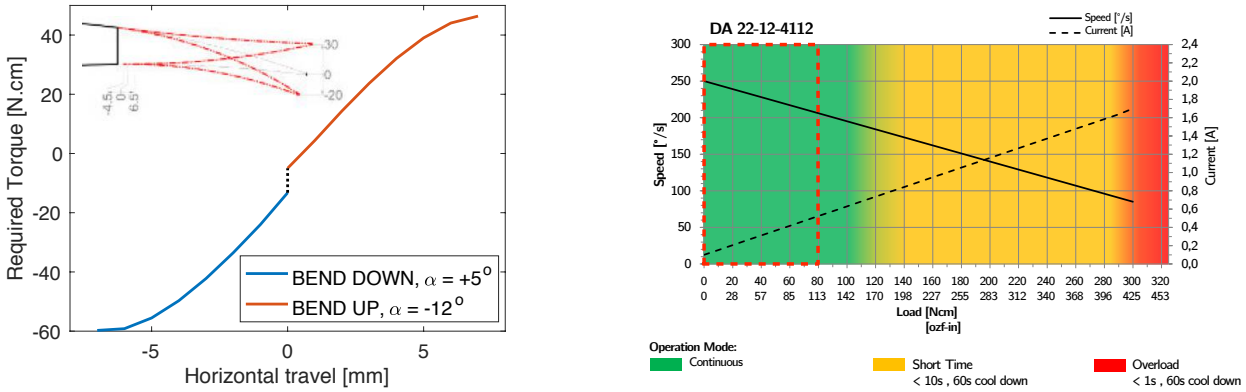

(a) Torque vs horizontal travel, bend up and down considered. (b) Volz DA-22-12-4112 performance parameters [21].

Fig. 9 Actuator torque and actuator selection for continuous torque requirement.

The analysis was conducted at 30 m/s. The angle of attack was maintained at +5° for bend down cases and -12° for bend up cases. From this analysis, the peak torque required to actuate all morphing shapes at V_∞ = 30 m/s is ±0.6 Nm. Furthermore, a dynamic bandwidth requirement, of 2 Hz actuation frequency at ±40 degrees servo arm rotation, was set to cope with the active manoeuvre load alleviation task. This yielded the following requirements for the actuator:

1) Deliver a peak torque of at least ±0.8 Nm.
2) Ability to operate this peak toque at 2 Hz at ±40 degrees servo arm rotation.

Volz DA 22-12-4112 servo was selected due to its high continuous load and position feedback capabilities. Fig. 9b shows the performance specification data of the actuator published by the manufacturer [21]. The green region indicates the range in which the servo can operate continuously. As seen, the peak torque requirement, indicated with a red-dotted box, falls within the continuous operation range of the servo.

C. Intermodular elastomeric skin

To allow adjacent morphing modules to actuate independently while ensuring that the wing surface remains smooth, it was decided to interconnect adjacent morphing modules with connecting segments.

The requirement for the connecting segments was to (i) preserve actuation and morphing authority, while not exceeding the continuous load requirements of the selected actuators, (ii) ability to sustain pressure loads for the

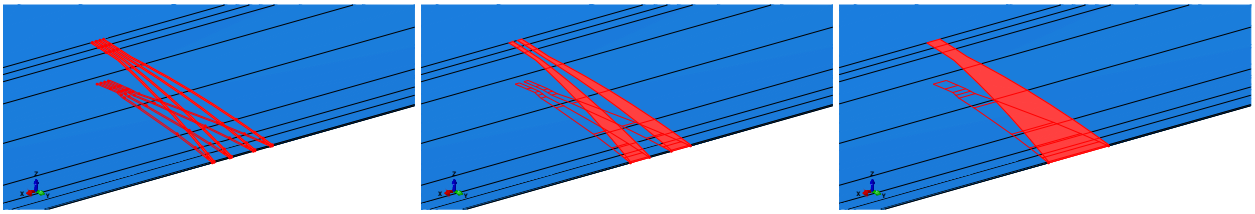

(a) High density slits filled with silicone. (b) Wider silicone patch reduced slit density. (c) Gap fully covered by silicone.

Fig. 10 Elastomer skin design concepts.

operational flow regimes (up to 50 m/s), (iii) allow post-manufacturing integration and (iv) ensure routing of cables from tip to root. In particular, concerning the third requirement, an elastomer skin material was selected as a connecting body due to its durability, ease of use and a good compromise between strength and durability [22].

A FE model was built in Abaqus to study the flexibility and the impact of the elastomer material on the actuation loads. Various skin patch designs were considered with silicone-filled slits of varying width and slit density, as shown in Fig. 10.

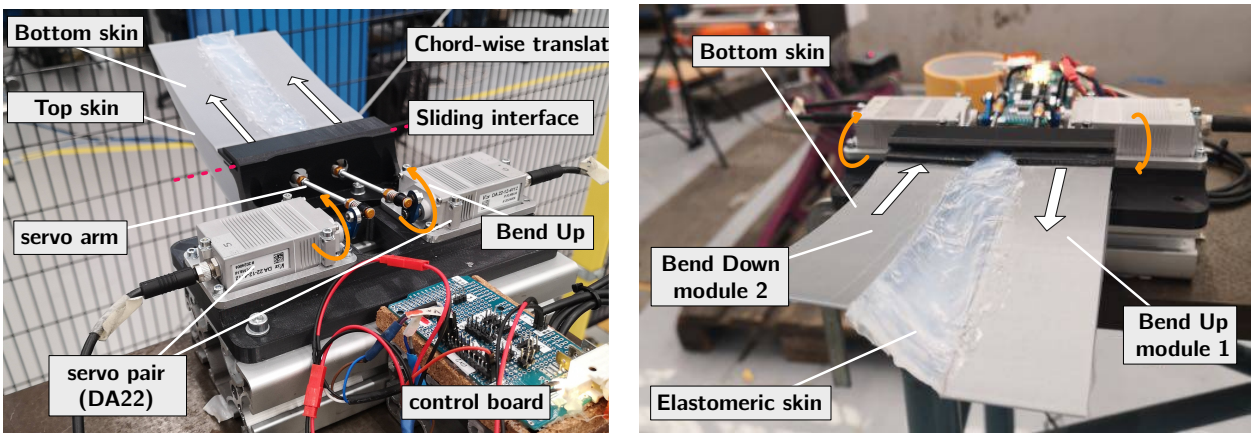

(a) Testing jig components. (b) Maximum limits between the adjacent modules with.

Fig. 11 Elastomer prototyping and testing jig.

The initial assessment led to gradually increasing the gap between the adjacent modules that was filled with the silicone. Further prototyping and testing using 3D printed jig confirmed the final elastomer design with a fully silicone-filled gap. The prototyping jig shown in Fig. 11 was actuated with two Volz DA-22-12-4112 servos and represented the connection between the adjacent modules. Fig. 11b shows the testing of the silicone for maximum deflection limits between the adjacent modules. The morphing modules were represented by the trailing edge section of the baseline NACA 6510 airfoil which were 3D printed from PLA (Polylactic Acid) plastic material. During the prototype testing various silicone skin samples from the Wacker Elastosil series [23] were considered. The moisture curing rubber silicone E41 from Wacker Elastosil series [24] was chosen as the best candidate based on a good compromise between flexibility and bonding durability after cyclic actuation tests were performed. The manufacturing process and the application of the silicone are shown in Fig. 12. Cuts were made in the top and bottom skin to facilitate the specified gap between adjacent modules. A temporary mould was made from 3D printed PLA (red component in Fig. 12) with a matching curvature of the airfoil to facilitate to hold silicone in-place while curing. The silicone was then applied, first on the top then bottom skin. Teflon tape was attached on the edges and the 3D printed mould to allow easy release of the cured silicone.

The integration of various technologies and active morphing design developed for the SmartX wing is demonstrated in static and dynamic wind-tunnel tests at the Open Jet Facility (OJF) at the Delft University of technology, equipped with a gust generator.

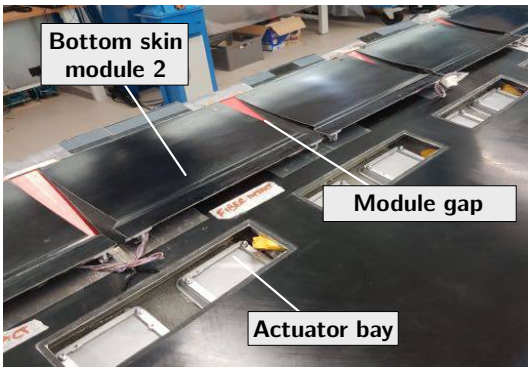

(a) Preparation of the cuts of the adjacent modules.

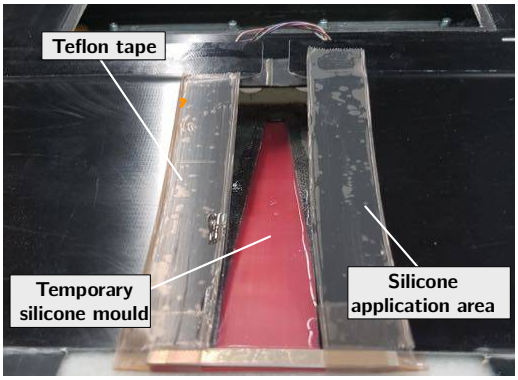

(b) Application process of the silicone.

Fig. 12 Manufacturing of the silicone skin segments.

V. Validation of the morphing design

To validate the conceptual design and assess the capability of the wing demonstrator to attain the static target morphing shapes, a Digital Image Correlation (DIC) static measurement was conducted on the top and bottom surface of the morphing modules.

A. DIC measurement setup and conditions

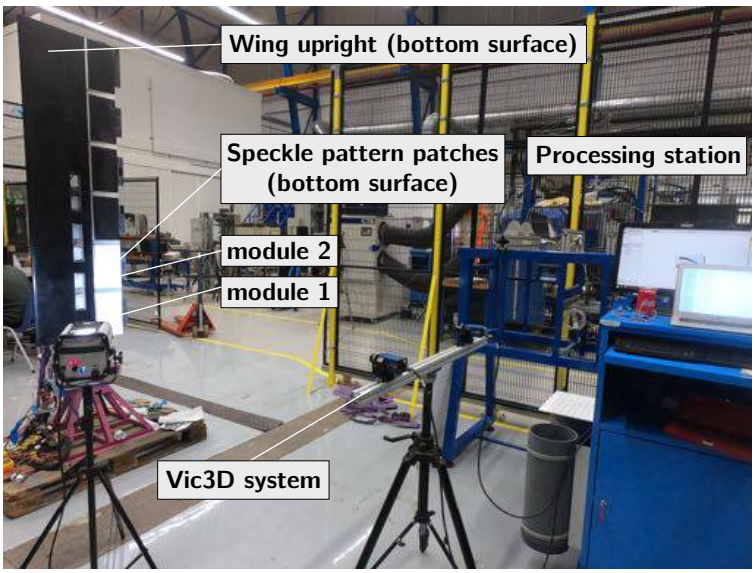

(a) Vic3D DIC measurements system.

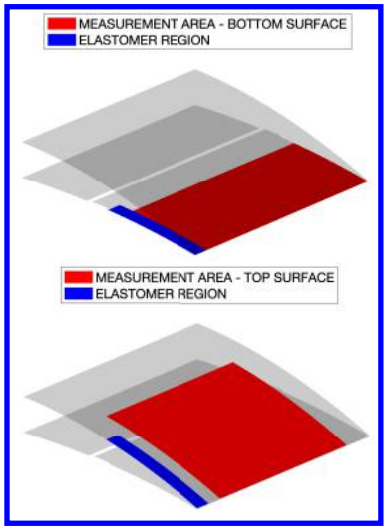

(b) Top and bottom DIC measurement area

Fig. 13 DIC measurements setup.

The DIC test setup is shown in Fig. 13. The measurement system consisted of a Vic-3D stereo Q400 system equipped with 15 mm lens [25]. The wing was placed upright and the top and the bottom skin of two morphing modules (modules 1 and 2) were covered in a speckle pattern. The areas where the deformations were measured are indicated by the red patches in Fig. 13b. On the lower surface, the trailing 130mm portion of the wing was analyzed. On the top surface, the trailing 190 mm portion of the wing was analyzed. The measurement area spanned 200 mm on the top surface in the spanwise direction and was centred on the module.

A measurement test matrix was designed to reflect the morphing design limits of the airfoil (shown in Tab. 2).

Table 2 DIC measurement test matrix.

Condition	Type [-]	Module 1 δ_1 [$\circ$]	Module 1 δ_2 [$\circ$]	Module 2 δ_1 [$\circ$]	Module 2 δ_2 [$\circ$]	step [$\circ$]
Bend Down	Symm.	-25	-25	-25	-25	5
Bend Up	Symm.	+25	+25	+25	+25	5
Differential Bend Down	Asymm.	-25	-25	+25	+25	5
Differential Bend Up	Asymm.	+25	+25	-25	-25	5

Maximum allowable actuation limits for both modules were chosen between positive 25 degrees and negative 25 degrees. The actuators were commanded in steps of 5 degrees according to the scheme in Tab. 2. In this table, a Bend Up and Bend Down manoeuvre of a single actuator, correspond to +25 and -25 degree actuation inputs, respectively. In total four cases were considered, (i) Bend Down, (ii) Bend Up, (iii) Differential Bend Down and Differential Bend Up (iv). In the symmetric arrangement, both modules moved in the same direction (both up or down) and in the asymmetric case the modules moved opposite to each other (one up and one down). The latter cases were designed to assess the impact of the elastomer skin on the morphed shape, as due to the differential actuation, stretching and shearing was expected to take place in the elastomer. The DIC static measurements were repeated twice for the symmetric case (trial 1 and trial 2) and compared with the prediction generated by the numerical model developed earlier. The numerical model did not include the elastomer skin, hence it is expected, that the numerical results show the best possible morphing case, where the elastomeric skin does not affect the morphing displacement of the module. The measurements for the asymmetric case were conducted similarly in two trials and compared to the symmetric cases.

B. Calibration and transformation

To be able to perform comparative analyses with the numerical model, the DIC measurements were transformed into the same reference frame used in the numerical model. This was done by orienting the trailing edge of the measured surfaces in line with the span-wise axis of the numerical model. A rotation about this axis was then performed to ensure the undeformed surfaces measured aligned with the undeformed analysis model. The DIC stereo camera setup was calibrated with a standard calibration target consisting of a 30mm circular grid pattern. Verification of the DIC calibration was conducted on the top surface by comparing the trailing edge tip deflections measured with DIC against deflections measured with a Vernier height gauge. Furthermore, repeatability assessment of the commanded morphed shape and the baseline shape in rest were performed. In both tests, the commanded actuator input configuration was found to generate a repeatable morphed shape. Similarly, assessment of the baseline shape was performed to ensure commanded shapes arrived at the same baseline in the unloaded case (at rest). This assessment was found to correspond well to the expected NACA 6510 airfoil.

C. Results

The comparison of the results between the DIC and the numerical model was made by comparing (i) the tip deflection, (ii) the 2D airfoil shape and (iii) heat maps of the out-of-plane and chord-wise displacements of the skin.

Fig. 14 shows tip deflection for the entire range of travel of the actuators in both symmetric as the asymmetric case.

1. Symmetric cases

Examining Fig. 14a for the symmetric case, the immediate observation yields that the linear curve predicted by the numerical model significantly overestimates the experimental tip deflection. The numerical model shows a linear slope between the actuator input range of [-25,25] degrees. While this linear trend seems to uphold, in the 0 to -25 degree range, the experimental curves have a much shallower slope compared to the prediction. On the opposite interval, the linear trend is less stable and trial 1, in contrast to trial 2, exhibits a dead-band between 0-5 degrees. Firstly, considering the slope mismatch, this suggests that a given actuator command may fall short to generate the desired camber change of the airfoil. Consequently, the morphed trailing edge, when subject to a free stream velocity, may fall short to deliver the maximum expected lift increment. Secondly, the dead-band and a higher uncertainty in the Bend Up case between the two trials suggest the actuation stroke may be partly consumed due to losses in the morphing actuation system.

Observing the out of plane deflections between the simulated and measured conditions in Fig. 15, the relative displacement gradient in the chord-wise direction is very similar, however, a noticeable bulging effect is occurring near

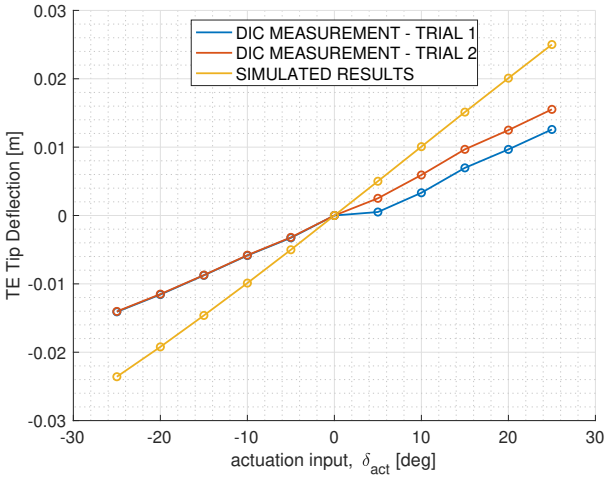

(a) Symmetric: tip deflections comparison DIC versus simulated full actuation range $[25, -25]$ **°.**

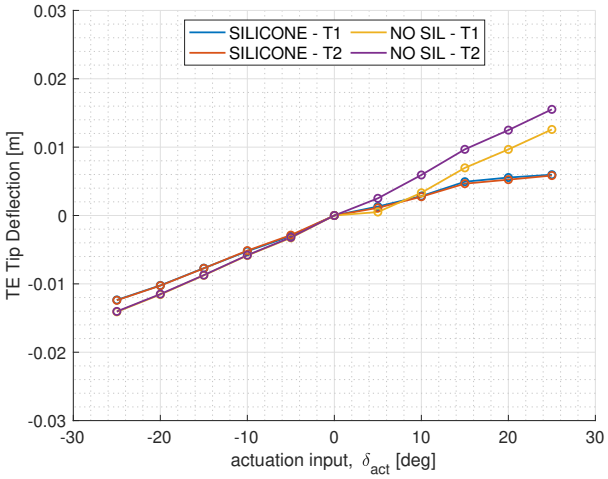

(b) Asymmetric: tip deflections and effect of silicone comparison DIC versus simulated full actuation range $[25, -25]$ **°.**

Fig. 14 DIC versus simulation tip deflection and the effect of the silicone.

the actuation areas on the bottom surface. Despite this effect, as the difference in magnitude is not drastic, this is not considered the primary cause of the discrepancy in the trailing edge tip deflection. Observing the chord-wise travel of the skin between measured and simulated results in Fig. 16 the cause of the trailing edge tip deflection is more apparent. It shows that the chord-wise travel of the bottom surface (top row) is nearly twice lower than expected. Kinematic interaction analysis of the actuator mechanism and sliding interface revealed that the actuation energy was largely consumed in the pivoting of a portion of the sliding surface and the stiff pickup body, instead of a purely chord-wise translation. This behaviour was also captured in the elastomer test setup as shown in the side view in Fig. 17. Although a limitation to the design, this can be partly overcome by adjusting the actuation input withing the allowable actuation

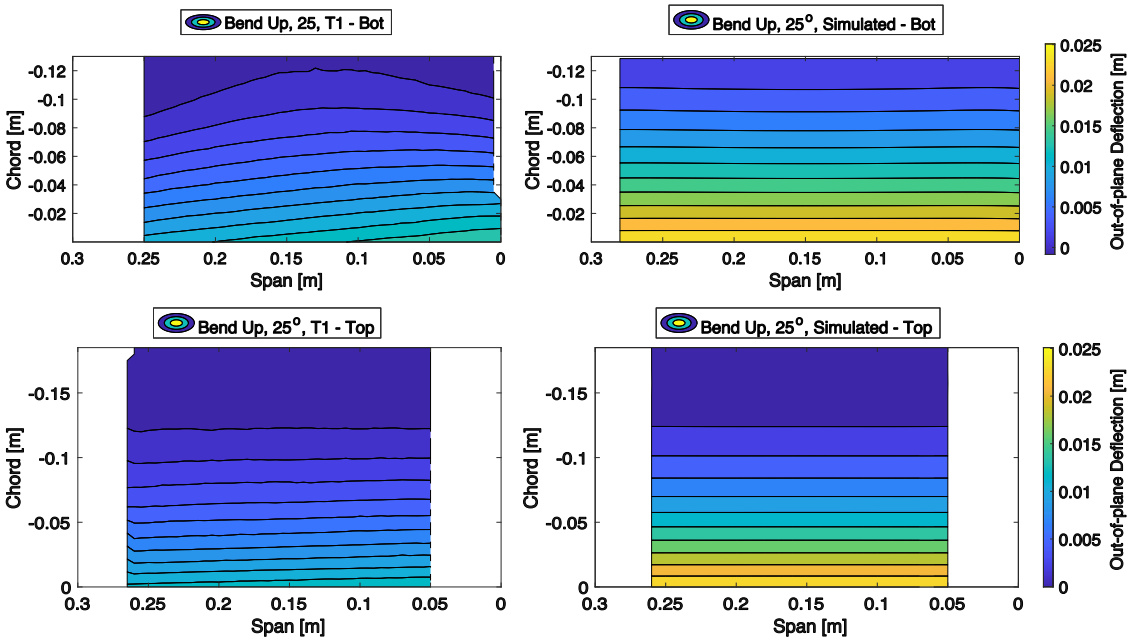

Fig. 15 Symmetric: Out-of-plane peak $(\pm 25°)$ **deflection comparison top and bottom view DIC versus simulated.**

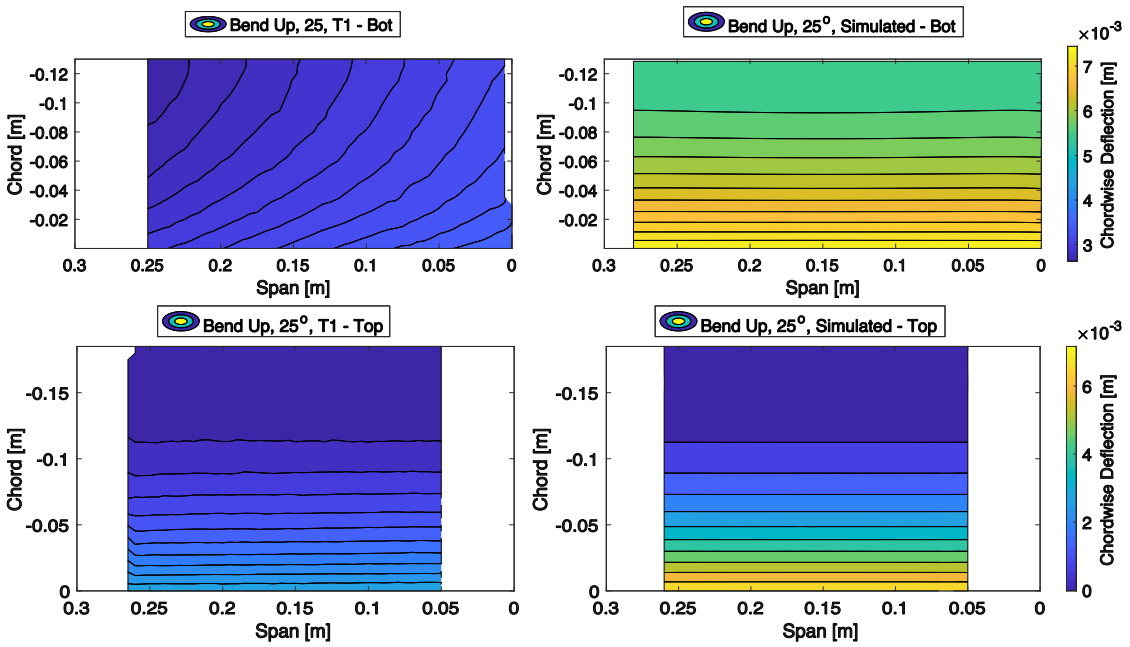

Fig. 16 Symmetric: chord-wise translation peak ($\pm 25°$) deflection comparison top and bottom view DIC versus simulated.

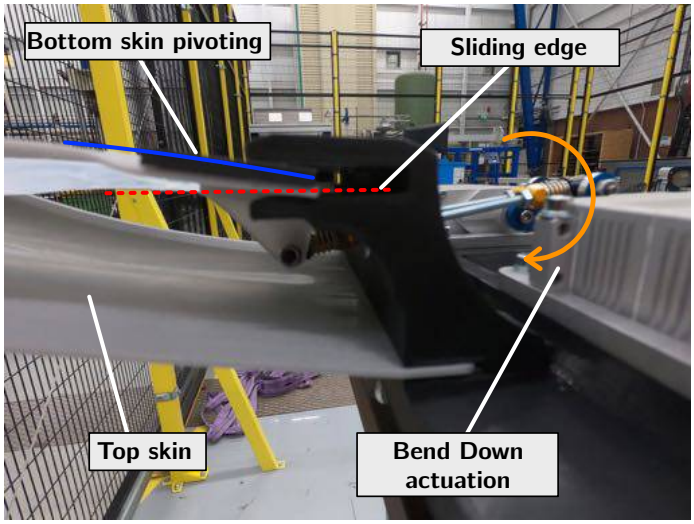

Fig. 17 Pivoting effect on the prototyping test jig.

range. More importantly, this finding provided valuable insight into the limitations of the design and helped to identify improvements for future designs. Observing Fig. 16 once again, the bottom skin in Fig. shows skewness in the gradient along the span that is not present in the numerical model. This is believed to be attributed to the boundary conditions present at the span extremities of the module, since, the left extreme is attached to module 2, and the right extreme is a free edge.

2. Asymmetric cases

Fig. 14b shows a comparison of the DIC measured tip deflections for the entire input range for symmetric and asymmetric cases where the modules were actuated in the opposite direction, generating tension and shearing in the elastomer skin. Observing, trials 1 and 2, corresponding to the blue and red line respectively, no dead-band is found

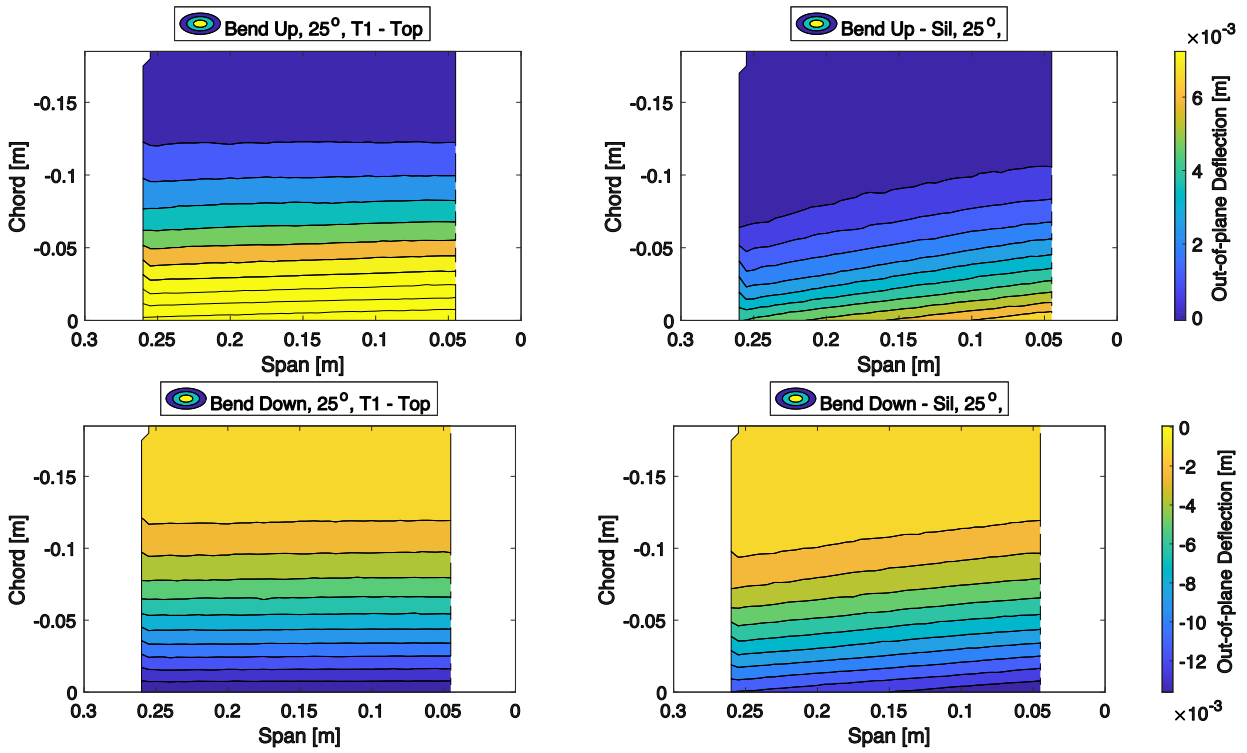

Fig. 18 Asymmetric and symmetric cases caparison: out-of-plane translation with and without silicone shearing on the top surface.

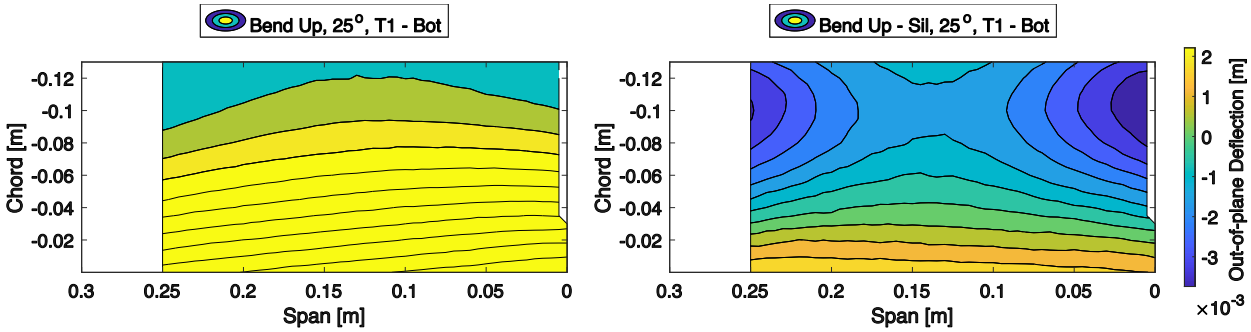

Fig. 19 Asymmetric and symmetric cases caparison: out-of-plane translation with and without silicone shearing on the bottom surface.

and the trials show a good agreement between each other. Furthermore, it is observed that tip deflection is reduced due to the shearing and stretching of the elastomer, as seen by a shallower slope. The interval between 0-25 degrees, corresponding to the module 1 bending upwards and module 2 downwards, shows the strongest impact of the elastomer. Here the tip deflections are significantly reduced.

Observing the out-of-plane deflection shown by the heat maps in Fig. 18 for trial 1 on the top surface, Bend Down (bottom row) shows reasonable agreement, however, in the Bend Up case the deformation are significantly reduced. The same measurement on the bottom surface, shown in Fig. 19 reveals a substantial bulging out effect. This suggests that as the stresses increase for peak deflection, rather than shearing the silicone skin, the actuation energy is consumed in bulging out of the skin. This also suggests that a better balance is needed between the elastomer stiffness and the wing skin stiffness to allow more shearing in the critical connecting areas.

3. Revised numerical model

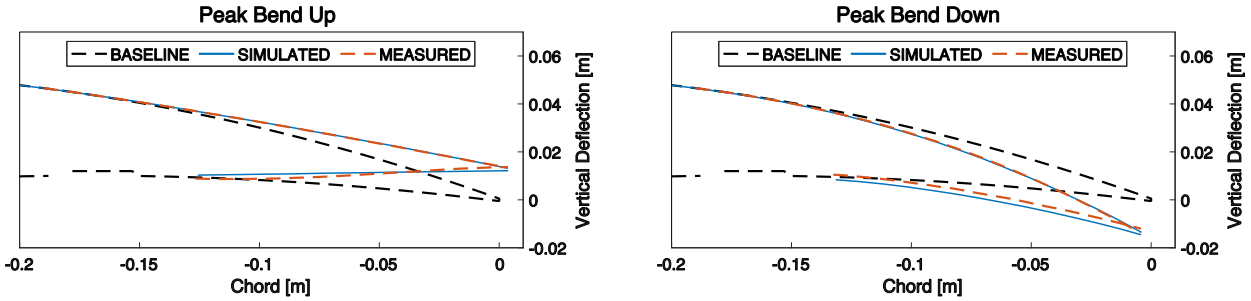

Fig. 20 Symmetric: peak deflections at ±25° comparison DIC versus simulated airfoil cross-section.

An attempt was made to revise the numerical model such that better prediction could be obtained for the morphing deflections. The numerical model was revised to include the actuation losses obtained from pivoting and bulging out effects. This was done by correcting the linear mapping between the actuator input and tip deflection. Fig. 20 shows the airfoil shape simulated for peak deflections with the revised model (blue line) at the right end of module 1. The revised model shows showed a good agreement with the DIC data (red line) between the symmetric peak Bend Up and Down cases. Further research is suggested to model the impact of elastomer skin on the morphing. This would help to refine the elastomer design to produce a more compliant seamless connection and limit the impact caused by shearing and stretching on the deflections.

VI. Conclusion

In this study, the design and development of an autonomous morphing wing concept are presented. This morphing wing is developed in the scope of the SmartX project, aiming to demonstrate in-flight performance optimisation of multiple objectives such as (i) drag optimisation, (ii) load alleviation, (iii) flutter suppression and (iv) shape control through multi-disciplinary utilisation of smart sensing, control, actuation and integration. A summary of the design steps is given leading to the development of the morphing wing and an analysis model. Various steps of the wing development are discussed and how the smart technologies are integrated into a hardware demonstrator subject to a wind tunnel test assessment. Furthermore, development and integration of the intermodular elastomeric skin are discussed, to allow seamless morphing between adjacent modules. The static performance of the morphing modules is analysed and validated using a DIC measurement system. Discrepancies are found between the deflection predictions of the analysis model and the DIC data. Analysis of the morphing skin deformations and kinematic assessment of the morphing actuation mechanism suggests that a significant portion of the actuator stroke is consumed in pivoting of the sliding surface attachment area. Furthermore, the effect of the elastomeric skin is assessed. The presence of the elastomeric skin is found to lead to lower tip deflections than predicted. The analysis model is revised to include a corrected mapping between actuator inputs and the tip deflections, which resulted in improved numerical predictions. Further research is recommended to include and model the impact of elastomer skin on the morphing. This would help to refine the elastomer design to produce a more compliant seamless connection and limit the impact caused by shearing and stretching on the deflections.

Acknowledgments

We would like to acknowledge Paul Lancelot for his assistance in understanding and implementing the NASTRAN SOL200 routine.

References

[1] Lentink, D., Müller, U. K., Stamhuis, E. J., De Kat, R., Van Gestel, W., Veldhuis, L. L., Henningsson, P., Hedenström, A., Videler, J. J., and Van Leeuwen, J. L., "How swifts control their glide performance with morphing wings," *Nature*, Vol. 446, No. 7139, 2007, pp. 1082–1085. https://doi.org/10.1038/nature05733.

[2] Bomphrey, R. J., Henningsson, P., and Hedenstro, A., "Efficiency of Lift Production in Flapping and Gliding Flight of Swifts," *PLoS ONE*, Vol. 9, No. 2, 2014. https://doi.org/10.5061/dryad.cn252.

[3] JEX, H., and CULICK, F., "Flight control dynamics of the 1903 Wright Flyer," *12th Atmospheric Flight Mechanics Conference*, American Institute of Aeronautics and Astronautics, Reston, Virigina, 1985, pp. –. https://doi.org/10.2514/6.1985-1804, URL http://arc.aiaa.org/doi/10.2514/6.1985-1804.

[4] Weisshaar, T. A., "Morphing aircraft systems: Historical perspectives and future challenges," *Journal of Aircraft*, Vol. 50, No. 2, 2013, pp. 337–353. https://doi.org/10.2514/1.C031456.

[5] Barbarino, S., Bilgen, O., Ajaj, R. M. R., Friswell, M. M. I., and Inman, D. D. J., "A review of morphing aircraft," *Journal of Intelligent Material Systems and Structures*, Vol. 22, No. 9, 2011, pp. 823–877. https://doi.org/10.1177/1045389X11414084.

[6] Vasista, S., De Gaspari, A., Ricci, S., Riemenschneider, J., Monner, H. P., and Van De Kamp, B., "Compliant structures-based wing and wingtip morphing devices," *Aircraft Engineering and Aerospace Technology*, Vol. 88, No. 2, 2016, pp. 311–330. https://doi.org/10.1108/AEAT-02-2015-0067.

[7] Previtali, F., Arrieta, A. F. A., and Ermanni, P., "Performance of a Three-Dimensional Morphing Wing and Comparison with a Conventional Wing," *AIAA Journal*, Vol. 52, No. 10, 2014, pp. 2101–2113. https://doi.org/10.2514/1.J052764, URL http://arc.aiaa.org/doi/10.2514/1.J052764.

[8] Molinari, G., Quack, M., Arrieta, A., Morari, M., and Ermanni, P., "Design, realization and structural testing of a compliant adaptable wing," *Smart Materials and Structures*, Vol. 24, No. 10, 2015. https://doi.org/10.1088/0964-1726/24/10/105027.

[9] Previtali, F., and Ermanni, P., "Performance of a non-tapered 3D morphing wing with integrated compliant ribs," *Smart Materials and Structures*, Vol. 21, No. 5, 2012. https://doi.org/10.1088/0964-1726/21/5/055008.

[10] Molinari, G., Arrieta, A., and Ermanni, P., "Aero-structural optimization of three-dimensional adaptive wings with embedded smart actuators," *AIAA Journal*, Vol. 52, No. 9, 2014, pp. 1940–1951. https://doi.org/10.2514/1.J052715.

[11] Jenett, B., Calisch, S., Cellucci, D., Cramer, N., Gershenfeld, N., Swei, S., and Cheung, K. C., "Digital Morphing Wing: Active Wing Shaping Concept Using Composite Lattice-Based Cellular Structures," *Soft Robotics*, Vol. 4, No. 1, 2017, pp. 33–48. https://doi.org/10.1089/soro.2016.0032, URL https://www.liebertpub.com/doi/10.1089/soro.2016.0032.

[12] Cramer, N. B., Cellucci, D. W., Formoso, O. B., Gregg, C. E., Jenett, B. E., Kim, J. H., Lendraitis, M., Swei, S. S., Trinh, G. T., Trinh, K. V., and Cheung, K. C., "Elastic shape morphing of ultralight structures by programmable assembly," *Smart Materials and Structures*, Vol. 28, No. 5, 2019, p. 055006. https://doi.org/10.1088/1361-665X/ab0ea2.

[13] Werter, N. P., Sodja, J., Spirlet, G., and De Breuker, R., "Design and experiments of a warp induced camber and twist morphing leading and trailing edge device," *24th AIAA/AHS Adaptive Structures Conference*, 2016. https://doi.org/10.2514/6.2016-0315, URL http://arc.aiaa.org.

[14] Mkhoyan, T., de Visser, C. C., and De Breuker, R., "Parallel Real-Time Tracking and 3D Reconstruction with TBB for Intelligent Control and Smart Sensing Framework," *AIAA Scitech 2020 Forum*, American Institute of Aeronautics and Astronautics (AIAA), 2020, p. 2252. https://doi.org/10.2514/6.2020-2252.

[15] Mkhoyan, T., de Visser, C. C., and De Breuker, R., "Adaptive Real-Time Clustering Method for Dynamic Visual Tracking of Very Flexible Wings," *AIAA Scitech 2020 Forum*, American Institute of Aeronautics and Astronautics (AIAA), 2020, p. 2250. https://doi.org/10.2514/6.2020-2250.

[16] Mkhoyan, T., Thakrar, N. R., De Breuker, R., and Sodja, J., "Design of a Smart Morphing Wing Using Integrated and Distributed Trailing Edge Camber Morphing," *ASME 2020 Conference on Smart Materials, Adaptive Structures and Intelligent Systems*, American Society of Mechanical Engineers, 2020, pp. –. https://doi.org/10.1115/smasis2020-2370, URL https://asmedigitalcollection.asme.org/SMASIS/proceedings/SMASIS2020/84027/Virtual,Online/1090388.

[17] Rodden, W. P., and Johnson, E. H., *MSC/NASTRAN aeroelastic analysis: user's guide; Version 68*, MacNeal-Schwendler Corporation, 1994.

[18] Drela, M., *XFOIL: an analysis and design system for low Reynolds number airfoils.*, 54), Berlin, Germany, Springer-Verlag, 1989, Springer-Verlag Wien, 1989.

[19] MSC Nastran, "MSC Nastran 2012 Design Sensitivity and Optimization User's Guide Main Index," Tech. rep., MSC Nastran, 2001. URL www.mscsoftware.com.

[20] Interglas, "Glass Filament Fabrics for Plastics Reinforcement - 92110 Product Specification," Tech. Rep. 0, Interglas, 2010.

[21] Volz, "Volz DA 22 Actuator Technical Specification," Tech. rep., Volz Servos GmbH, 2013.

[22] Thill, C., Etches, J., Bond, I., Potter, K., and Weaver, P., "Morphing skins," *The aeronautical journal*, Vol. 112, No. 1129, 2008, pp. 117–139.

[23] Chemie, Wacker and Hanns-Seidel-Platz, A G, "OVERVIEW OF ELASTOSIL ® GRADES SILICONE RUBBER FOR THE APPLIANCE INDUSTRY CREATING TOMORROW'S SOLUTIONS," Tech. rep., Wacker, 2020. URL www.wacker.com.

[24] Wacker, "ELASTOSIL ® E41 TRANSPARENT," Tech. rep., Wacker, 2020. URL http://www.wacker.

[25] Correlated Solutions, "VIC-3D 9 with iris System Specifications VIC-3D 9 System Specifications," Tech. rep., Correlated Solutions, 2020.